Supporting Information for

Mössbauer and DFT Study of the Ferromagnetically Coupled Diiron(IV) Precursor to a Complex with an $Fe^{IV}_2O_2$ Diamond Core

Marlène Martinho[†], Genqiang Xue[‡], Adam Fiedler[‡], Emile L. Bominaar[†], Larry Que Jr. [‡], Eckard Münck[†]

Contribution from the Department of Chemistry, Carnegie Mellon University, Pittsburgh, Pennsylvania, 15213 and Department of Chemistry and Center for Metals in Biocatalysis, University of Minnesota, 207 Pleasant Street SE, Minneapolis, MN 55455

Mössbauer analysis of the $[LFe^{IV}(O)(NCMe)]^{2+}$ complex.

An independent sample of $[LFe^{IV}(O)(NCMe)](OTf)_2$ was prepared by adding 1 equivalent of peracetic acid to a 1mM acetonitrile solution of $[L^{57}Fe^{II}(NCMe)](OTf)_2$. The zero field Mössbauer spectrum of $[LFe^{IV}(O)(NCMe)]^{2+}$ is shown Figure S1A. The red solid line represents a spectral simulation obtained by adding two quadrupole doublets with $\Delta E_{Q1} = 0.95(3)$ mm·s^{-1}, $\delta_1 = 0.00(2)$ mm·s^{-1} (doublet 1, ≈ 50%), and $\Delta E_{Q2} = 1.49(2)$ mm·s^{-1}, $\delta_2 = 0.45(1)$ mm·s^{-1} (doublet 2, ≈ 46%). The doublet 2 has an isomer shift typical for a high-spin Fe^{III} species. In applied magnetic fields, this species exhibits diamagnetic behavior and can be described as a diiron(III) complex (diiron(III) is often the thermodynamic sink in this chemistry). After subtraction of the doublet 2 (Figure S1B), doublet 1 is obtained with parameters typical of $Fe^{IV}(O)$ complexes.[1] The Mössbauer spectra of $[LFe^{IV}(O)(NCMe)]^{2+}$ were also recorded at 4.2 K in parallel applied fields up to 8.0 T, as well as 8.0 T spectra at 30 K and 100 K (Figures S2 and S3).

We have simulated the spectra of $[LFe^{IV}(O)(NCMe)]^{2+}$ using the S = 1 spin Hamiltonian:

$$\hat{\mathcal{H}} = D(\hat{S}_z^{\,2} - \tfrac{2}{3}) + E(\hat{S}_x^{\,2} - \hat{S}_y^{\,2}) + 2\beta \mathbf{B}\cdot\hat{\mathbf{S}} + \hat{\mathbf{S}}\cdot\mathbf{A}\cdot\hat{\mathbf{I}} - g_n\beta_n \mathbf{B}\cdot\hat{\mathbf{I}} + \hat{\mathcal{H}}_Q$$

$$\hat{\mathcal{H}}_Q = \left(\frac{eQV_{zz}}{12}\right)\left(3\hat{I}_z^{\,2} - \tfrac{15}{4} + \eta\left(\hat{I}_x^{\,2} - \hat{I}_y^{\,2}\right)\right)$$

$$\Delta E_Q = \left(\frac{eQV_{zz}}{2}\right)\left(1 + \frac{\eta^2}{3}\right)^{1/2}$$

The parameters obtained are listed in Table S1.

Table S1. Experimental and DFT-calculated Mössbauer parameters of $[LFe^{IV}(O)(NCMe)]^{2+}$.[a]

	$A_x/g_n\beta_n$ (T)	$A_y/g_n\beta_n$ (T)	$A_z/g_n\beta_n$ (T)	ΔE_Q (mm/s)	η	δ (mm/s)
Exp.	-23.0	-23.0	-4.0	+0.95	0.8	0.0
Calc.[b]	-21.1	-23.1	-5.6	+0.94	0.8	0.05

[a] The calculated A-values were obtained from the calculated A_{SD} values, by adding the experimental $A_{iso} = -16.6$ T.
[b] With B3LYP/6-311G, using G'03.

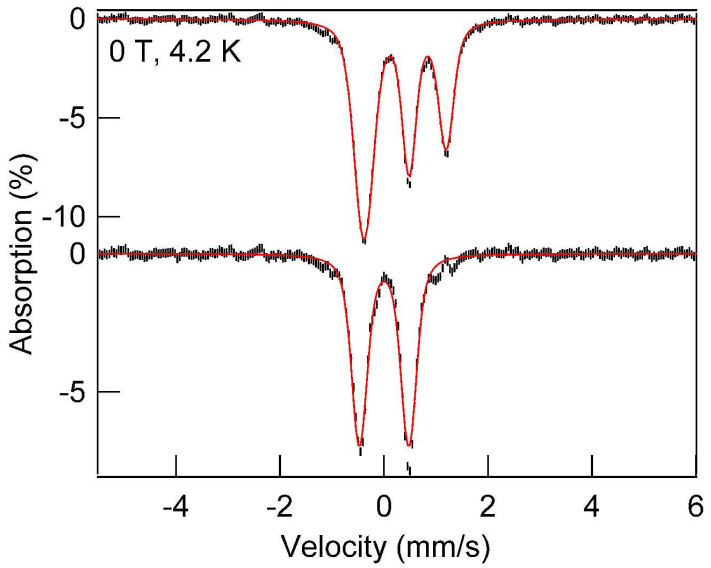

Figure S1. (A) 4.2 K Mossbauer spectrum of $[LFe^{IV}(O)(NCMe)]^{2+}$ generated by adding 1 equivalent of peracetic acid to $[L^{57}Fe^{II}(NCMe)](OTf)_2$ in MeCN (B) spectrum obtained after subtraction of 46 % of a diferric component from the raw data. The solid line in (A) is a spectra simulation containing ≈ 50% of $[LFe^{IV}(O)(NCMe)]^{2+}$ and ≈ 46% of the diferric species. The red solid line in (B) is a spectral simulation for the $[LFe^{IV}(O)(NCMe)]^{2+}$ component, using $\Delta E_{Q1} = 0.95$ mm/s and $\delta_1 = 0.00$ mm/s.

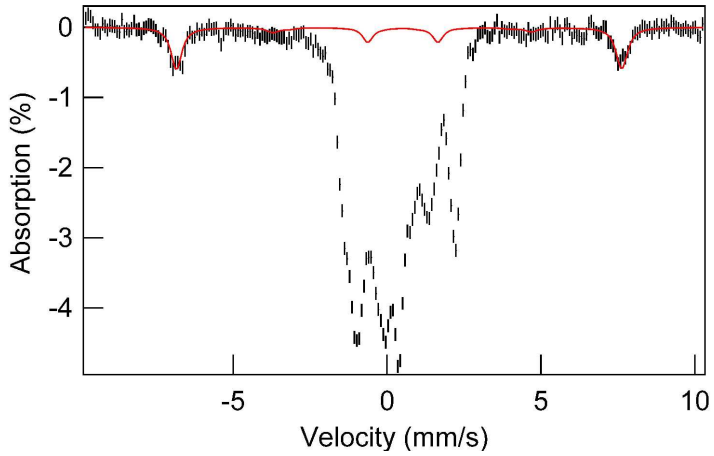

Figure S2. 4.2 K Mössbauer spectrum of $[LFe^{IV}(O)(NCMe)]^{2+}$ generated by adding 1 equivalent of peracetic acid to $[L^{57}Fe^{II}(NCMe)](OTf)_2$ in MeCN, recorded in an 8.0 T field applied parallel to the observed γ radiation. The red line is a spectral simulation of high-spin Fe^{3+} contaminants representing ≈ 8% of the iron in the sample.

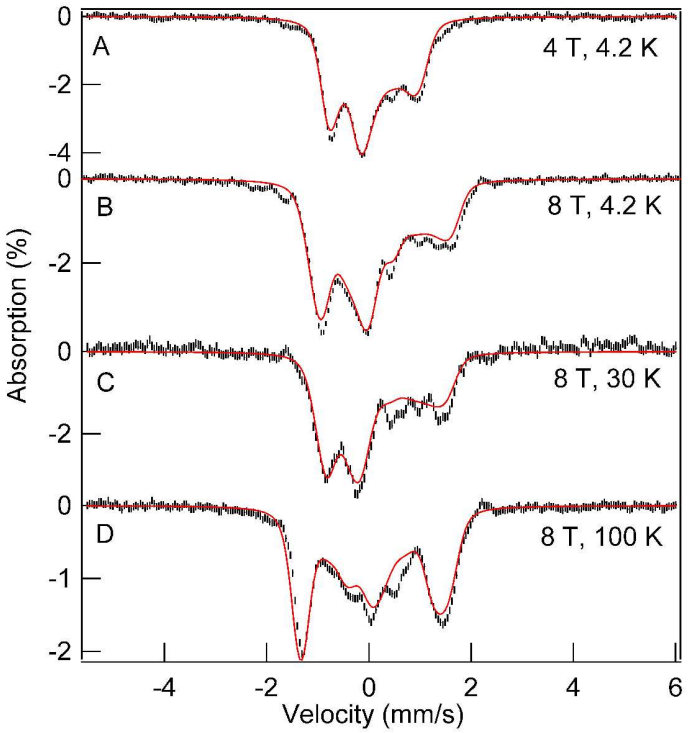

Figure S3. Mössbauer spectra of $[LFe^{IV}(O)(NCMe)]^{2+}$ generated by adding 1 equivalent of peracetic acid to $[L^{57}Fe^{II}(NCMe)](OTf)_2$ in MeCN. The spectra were recorded in 4.0 T (A) and 8.0 T (B, C, D) applied parallel to the γ ray at temperatures as indicated. The spectra were obtained after subtraction of the 46% of the diiron(III) species. The red solid lines are spectral simulations to an S = 1 spin Hamiltonian using the parameters listed in Table S1.

DFT-analysis of the $[LFe^{IV}(O)(NCMe)]^{2+}$ complex.

The density functional theory (DFT) calculations for $[LFe^{IV}(O)(NCMe)]^{2+}$ was performed using Becke's three parameter hybrid functional (B3PLY) and basis set 6-311G provided by Gaussian'03 software package.[2] The quadrupole splitting ΔE_Q was calculated using the properties keyword of the Gaussian code using $\alpha(^{57}Fe) = 0.17$ barn. The ^{57}Fe isomer shift δ was evaluated from the DFT charge density at the Fe nucleus using the calibration given by Vrajmasu et al.[3] The SCF procedure and geometry optimization were terminated upon reaching the default convergence criteria (Figure S4). The calculated Fe-O bond distance is 1.65 Å, which agrees with the Fe-O bond distances for other S=1 $Fe^{IV}(O)$ complexes.[1, 4] The DFT-calculated Mössbauer parameters agree quite well with the experimental data (Table S1).

We also optimized the geometry of the structure of $[LFe^{IV}(O)(NCMe)]^{2+}$ where the oxo and MeCN groups have been exchanged (not shown), leading to a structure with the oxo group *trans* to a N_{py} and the MeCN group *trans* to N_{am}. This conformation is 2400 cm^{-1} higher in energy.

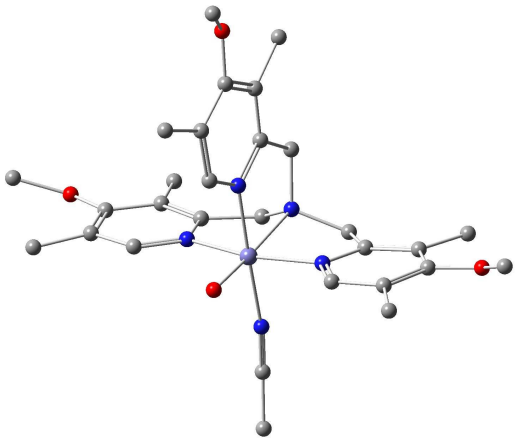

Figure S4. Geometry optimized structure of the $[LFe^{IV}(O)(NCMe)]^{2+}$ complex. Hydrogen atoms have been omitted for clarity.

Supplemental information on the Mössbauer analysis of complex **2**.

The spectrum in Figure S5 contains two quadrupole doublets assigned to **2** and diferric components (≈ 35% of total Fe). As only 0.8 equiv. peroxide were used, it is reasonable to assume that ca. 20% of the Fe in the sample belongs to **1**. Roughly 10% of the absorption may be attributable to diferric decay product(s) and a starting material contaminant, and since these diferric species yield spectra quite similar to those of **1**, we have represented the spectra of all diferric species, for lack of better information, by the spectrum of **1**. Ca. 5% of the iron in the sample belonged to green intermediate **4**; its contribution was determined by EPR and by comparing Mössbauer spectra recorded at 4.2 K and 100 K. Throughout the project we have searched for a method, other than Mössbauer spectroscopy, to determine the fraction of **2** in a sample, and we found that the amount of red intermediate **3** obtained by protonation correlates very well with the

Mössbauer analysis. For instance, for an aliquot of the present Mössbauer sample 65% of the starting material, upon protonation, was converted into **3**. We have produced one sample containing ca. 75% of **2**; however, for this sample ca. 10% of the iron belonged to a heterogeneous mixture of paramagnetic high-spin ferric contaminants displaying spectral features that were difficult to recognize in high-field spectra.

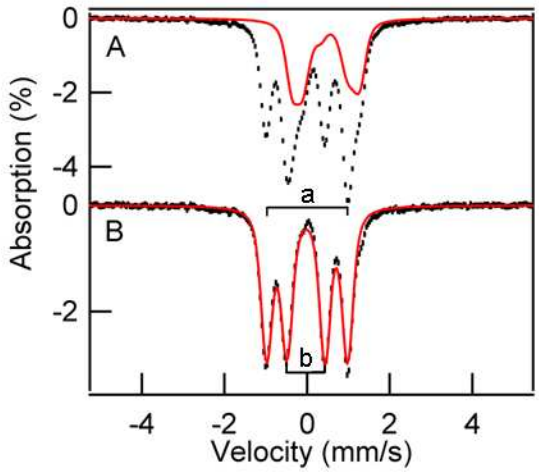

Figure S5. Mössbauer spectrum (A) of **2** in 1:1 mixture of acetonitrile/butyronitrile, recorded at 4.2 K in zero field. The solid line is a spectral simulation of the diferric contaminants. (B) Spectrum of **2** obtained by subtracting the contaminants of (A) from the raw data.

We have measured the spectra of **2** for B = 0 up to 190 K and found that the intensity of doublet **a** (relative to **b**) and also its quadrupole splitting decrease with increasing temperature (Figure S6), and these changes are accompanied by a broadening of the lines, caused by dynamic effects perhaps involving the OH group of site **a**. As we were writing up this manuscript, we prepared a sample of **2** using D_2O_2; see Material and Methods. An initial Mössbauer study of that sample gave a very interesting result, namely that the recoilless fraction (Debye-Waller factor), f, of site **a** declines substantially faster above 100 K than the f-value of site **b**.[5] The decline in f is illustrated in Figure S6 which shows

a superposition of 4.2 K and 140 K spectra of the D_2O_2 sample. At 140 K we find for doublets **a** and **b** an intensity ratio [**b**]/[**a**] = 1.4 rather than 1:1 as observed at 4.2 K. We have reported a similar, but less dramatic, phenomenon for the Fe^{2+} site of the P-cluster of nitrogenase.[6] We will study the high-temperature behavior more thoroughly with both EXAFS and Mössbauer spectroscopy, and report the results elsewhere. Interestingly, the sample prepared with D_2O_2 did not suffer from line broadening above 100 K. Given that the high temperature spectra of the sample of Figures 2 and 3 consist of a superposition of at least seven quadrupole doublets with unknown high-temperature behavior, we are presently not able to properly decompose the spectra.

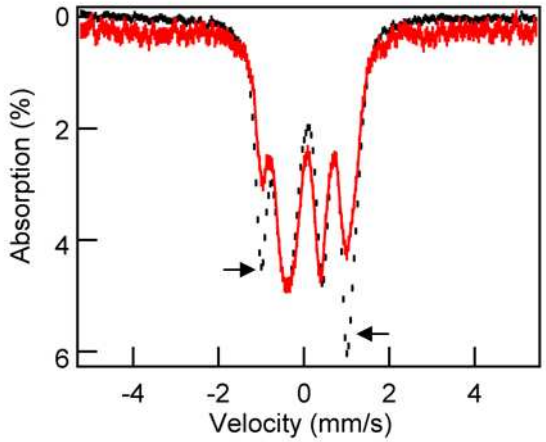

Figure S6. Comparison of the 4.2 K (black) and 140 K (red) spectra of a sample of **2** prepared with D_2O_2. 74% of the Fe in the sample belongs to **2** and ca. 25% to diferric species. At 4.2 K, doublet **a** (arrows) accounts for ca. 37% of the total absorption; this fraction declines to 28 % of the total absorption at 140 K. The average recoilless fraction declines by a factor 2 between 4.2 K and 140 K; the recoilless fraction of doublet **a** declines by nearly a factor 3. Vertical scale refers to 4.2 K spectrum.

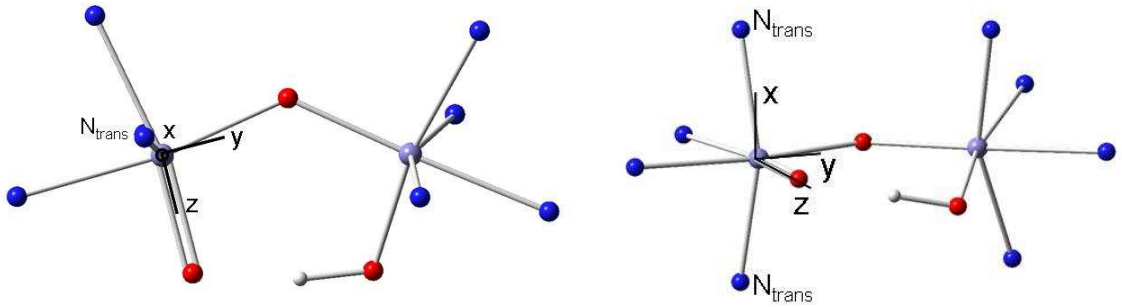

Figure S7. Representation of the coordinate frame {x, y, z} of the Fe_O site of **2** viewed from two perspectives; the z axis is along the Fe=O bond and the x axis is along the N_{trans}---N_{trans} direction on the Fe_O site. Left: view from top along the x axis; right: view from the front of the molecule. Atom colors: blue, nitrogen; red, oxygen; grey, iron; white, hydrogen. Except for the coordinating atoms, the ligands have been omitted for clarity.

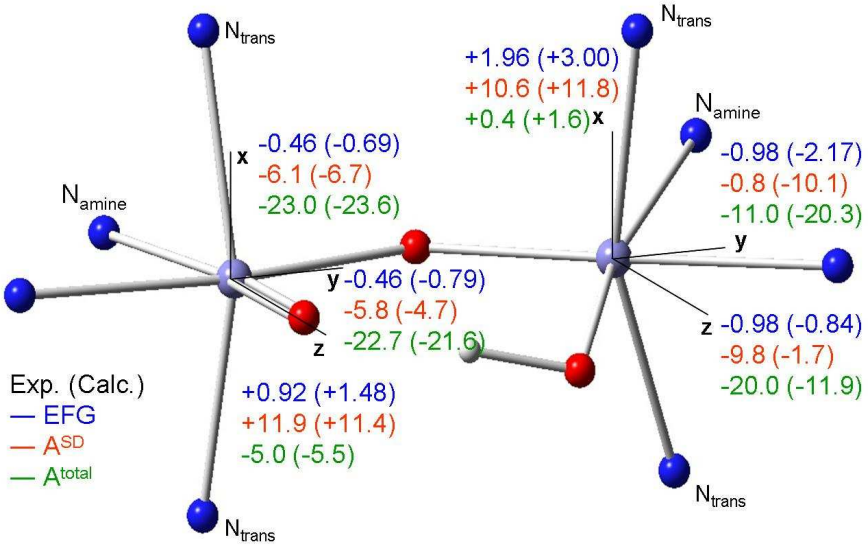

Figure S8. Representation of the experimental and DFT-calculated principal values of the EFG- (in mm/s), A_{SD}- and A_{total} -tensors (in T) (opt, *method 1*; prop, *method 2*) using the coordinate frame of the Fe_O site, {x, y, z}, as a reference, where the z axis is along the Fe_O-O_T bond and the x axis is along the N_{trans}---N_{trans} direction on the Fe_O site. The principal axes of the EFG and A_{SD} tensors at Fe_{OH} are close to but do not coincide with the {x, y, z} axes. Atom colors: blue, nitrogen; red, oxygen; grey, iron; white, hydrogen.

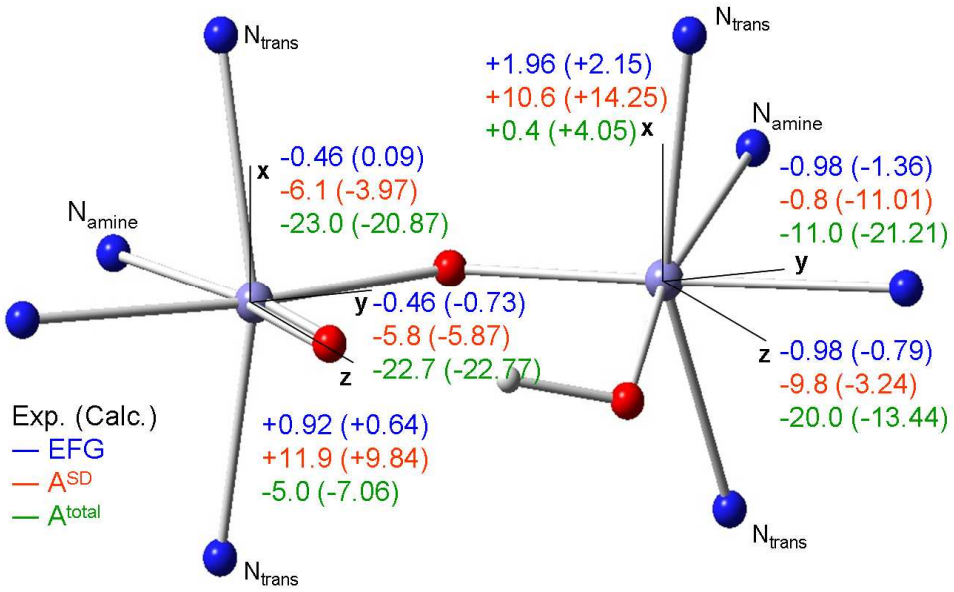

Figure S9. Representation of the experimental and DFT-calculated principal values of the EFG- (in mm/s), A_{SD}- and A_{total} -tensors (in T) by (both opt and prop, *method 1*) using the coordinate frame of the Fe_O site, {x, y, z}, as a reference, where the z axis is along the Fe_O-O_T bond and the x axis is along the N_{trans}---N_{trans} direction on the Fe_O site. The principal axes of the EFG and A_{SD} tensors at Fe_{OH} are close to but do not coincide with {x, y, z} axes (see main text). Atom colors: blue, nitrogen; red, oxygen; grey, iron; white, hydrogen.

Comments on DFT Calculations for Complex **2**.

Methods.

Density functional theory (DFT) calculations were performed for complex **2** and for the analog of complex **2** supported by a truncated version of the ligand, tris(pyridyl-2-methyl)amine (TPA), where the substituents on the pyridyl rings have been replaced by H.

Method 1: calculations were performed with the Amsterdam Density Functional (ADF) 2008.01 software package[7] on a cluster of 10 processors (Ace computers) using ADF basis set IV (triple-ζ with single polarization on the ligand atoms), an integration constant of 4.0, and the Vosko-Wilk-Nusair local density approximation[8] with the nonlocal

gradient corrections of Becke[9] and Perdew[10] (BPVWN). The coordinates of the optimized geometry are reported in Table S12. A-tensor and electric field gradient calculations in ADF were performed using the ESR and QTENS commands, respectively. Spin-orbit contributions to the A-tensor were neglected. The EFG has been converted to energy units, using Q(^{57}Fe) = 0.17 barn. Since the calculations employed basis sets with frozen cores, the resulting A_{iso} values (Fermi contact term) were meaningless; however, it was still possible to extract the spin-dipolar terms by subtraction of A_{iso} from the computed **A**-tensor. Finally, since ADF assumed an effective spin of 2, the calculated values are divided by 2 to obtain the local A-values.

Method 2: calculations were performed using Becke's three parameter hybrid functional (B3LYP)[11, 12] and basis set 6-311G provided by Gaussian'03 software package[2] on a cluster of 8 processors.[13] The quadrupole splitting ΔE_Q was calculated using the properties keyword of the Gaussian code and Q(^{57}Fe) = 0.17 barn. The ^{57}Fe isomer shift δ was evaluated from the DFT charge density at the Fe nucleus using the calibration given by Vrajmasu et al.[3] The SCF procedure and geometry optimization were terminated upon reaching the default convergence criteria. The populations were calculated with the Population keyword.

Method 3: One calculation was performed in the same way as *Method 2* but using the PBEVWN functional instead of B3LYP.

Description of the DFT Results.

In Table S2 we present the experimental and calculated values for the magnetic hyperfine coupling constants, quadrupole splittings, and asymmetry parameters for the two iron sites in complex **2**. Since, in our experience, *method 2* underestimates the value of the Fermi contact term in high-valent iron species, we have only calculated the spin-dipolar contribution to the magnetic hyperfine parameters. The A_{SD} values were added to A_{iso}, the average over the experimental hyperfine coupling constants, to obtain the A values listed as "calculated" in Table S2. The principal values of the EFG and A tensors have been assigned to the axes in Figures S8 and S9 (see below for discussion of axes).

Table S2. Experimental and DFT-calculated Mössbauer parameters for the Fe_O and Fe_{OH} sites of **2**.[a,b]

		opt[b,c]	prop[b,d]	$A_x/g_n\beta_n$ (T)	$A_y/g_n\beta_n$ (T)	$A_z/g_n\beta_n$ (T)	ΔE_Q (mm/s)	η
Fe_O	Exp.	-	-	-23.0	-22.7	-5.0	+0.92	0
	Calc.[a]	1	2	-23.6	-21.6	-5.5	+1.57	0.07
		1	1	-20.9	-22.8	-7.1	-0.80	0.75
Fe_{OH}	Exp.	-	-	+0.4	-11.0	-20.0	-1.96	-3
	Calc.[a]	1	2	+1.6	-20.3	-11.9	+3.29	0.44
		1	1	+4.0	-21.2	-13.4	+2.18	0.27

[a] The calculated A values have been obtained by adding the experimental values A_{iso} = -16.9 and -10.2 T for the Fe_O and Fe_{OH} sites, respectively, to the A_{SD} values calculated for these sites (Table S9).
[b] Optimization used functional/basis (code): 1 = BPVWN/IV (ADF), 2 = B3LYP/6-311G (G'03).
[c] Method used for geometry optimization.
[d] Method used for calculation of properties.

Table S3. Population of *d* orbitals for Fe_O and Fe_{OH} sites of **2**.[a]

Site	opt[b,c]	prop[b,d]	d_{xy}	d_{x2-y2}	d_{xz}	d_{yz}	d_{z2}
Fe_O	1	2	1.89	0.67	1.37	1.29	0.87
Fe_{OH}	1	2	1.43	0.75	1.30	1.80	0.78
Fe_O	1	1	1.73	0.90	1.41	1.42	0.92
Fe_{OH}	1	1	1.51	0.91	1.49	1.67	0.86
Fe_O	2	2	1.92	0.63	1.37	1.35	0.85
Fe_{OH}	2	2	1.36	0.76	1.86	1.28	0.80

[a] The orbital frame of the Fe_O site, x ∥ N_t-N_t, y ∥ Fe_O-O_B, z ∥ Fe_O-O_T; orbital frame of the Fe_{OH} site: x ∥ N_t-N_t, y ∥ Fe_{OH}-O_B, z ∥ Fe_{OH}-O_H (cf. Figure 6 in the main text).
[b] Optimization used functional/basis (code): 1 = BPVWN/IV (ADF), 2 = B3LYP/6-311G (G'03).
[c] Method used for geometry optimization.
[d] Method used for calculation of properties.

Table S4. Spin population of *d* orbitals for Fe_O and Fe_{OH} sites of **2**.[a]

Site	opt[b,c]	prop[b,d]	d_{xy}	d_{x2-y2}	d_{xz}	d_{yz}	d_{z2}
Fe_O	1	2	0.07	0.09	0.61	0.66	0.06
Fe_{OH}	1	2	0.44	0.12	0.67	0.14	0.07
Fe_O	1	1	0.21	0.10	0.59	0.52	0.06
Fe_{OH}	1	1	0.37	0.11	0.49	0.27	0.06
Fe_O	2	2	0.03	0.08	0.60	0.63	0.04
Fe_{OH}	2	2	0.62	0.09	0.11	0.67	0.11

[a] The orbital frame of the Fe_O site, x ∥ N_t-N_t, y ∥ Fe_O-O_B, z ∥ Fe_O-O_T; orbital frame of the Fe_{OH} site: x ∥ N_t-N_t, y ∥ Fe_{OH}-O_B, z ∥ Fe_{OH}-O_H (cf. Figure 6 in the main text).
[b] Optimization used functional/basis (code): 1 = BPVWN/IV (ADF), 2 = B3LYP/6-311G (G'03).
[c] Method used for geometry optimization.
[d] Method used for calculation of properties.

Tables S3 and S4 list the total population and spin population of the individual 3d orbitals at Fe_O and Fe_{OH}. The Mulliken populations have been evaluated for the SCF solution obtained with the method listed in the column labeled "prop", using the structure obtained by geometry optimization with the method indicated in the column labeled "opt".

The spin density at Fe_O is consistently accommodated by the d_{xz} and d_{yz} orbitals. The populations of these obitals are significantly larger than 1 (Table S3) due to large covalent donation of electron density from O_T into these orbitals, resulting in spin populations that are less than 1 (Table S4). Orbital d_{xy} is essentially doubly occupied, as in mononuclear S = 1, Fe^{IV}=O species.[14, 15] The results for the Fe_{OH} site are more ambiguous. The unpaired electrons are in d_{xy} and d_{xz} in the optimized structure obtained with *method 1* and in d_{xy} and d_{yz} in the optimized structure obtained with *method 2*. The change results from a rearrangement of the t_{2g} orbitals caused by methodological differences in the dihedral angles for the core, notably in the one describing the orientation of the hydroxo group (see below).

The irons in complex **2** have mixed 4N-2O coordinations, including 1 amine (N_{am}) and 3 pyridines (N_{py}) (1 in-plane and 2 axial pyridines) at each site, 1 bridging oxo (O_B), and 1 terminal oxo (O_T) at one site and a terminal hydroxo (OH) at the other. Since O_B occupies a position that is, respectively, *trans* to N_{am} and N_{py} relative to the two irons, O_T must be *trans* to either N_{py} or N_{am}; accordingly, OH must be *trans* to N_{am} or N_{py}, respectively.

We did DFT calculations for the two isomers, $[L(O_T)_{am}FeO_BFe(OH)_{py}L]^{3+}$ and $[L(O_T)_{py}FeO_BFe(OH)_{am}L]^{3+}$ using *methods 1* and *2*. These calculations were performed for a complex based on the truncated ligand (L = TPA instead of SR_3TPA), in which the pyridine side chains were replaced by hydrogens. Tables S5 and S6 list selected distances, dihedrals, and bond angles for the two isomers obtained with the two methods. *Method 2* shows that the $[L(O_T)_{am}FeO_BFe(OH)_{py}L]^{3+}$ isomer (isomer A) is lowest in energy by a margin of 436 cm^{-1}. Most parameters show only minor variations. The most conspicuous change is in the Fe_O-N_{tr} distance (N_{tr} is *trans* to O_T), suggesting a *trans*

effect as the origin of the energy difference between the two isomers. Interestingly, *method 1* shows that the isomer $[L(O_T)_{py}FeO_BFe(OH)_{am}L]^{3+}$ (isomer B) is lowest in energy by 1000 cm^{-1}.

Table S5. Selected distances (in Å) for DFT optimized structures for the S = 2 states of the isomers $[L(O_T)_{py}FeOFe(OH)_{am}L]^{3+}$ and $[L(O_T)_{am}FeOFe(OH)_{py}L]^{3+}$ (L = TPA).

iso	opt[a]	Fe_O-O_T	Fe_O-N_{tr}	$<Fe_O$-$N_{py}>_{av}$[d]	Fe_O-O_B	Fe_{OH}-O(H)	Fe_{OH}-N_{tr}	$<Fe_{OH}$-$N_{py}>_{av}$	Fe_{OH}-O_B	Fe-Fe	(O)H···O_T
A[b]	2	1.653	2.123	2.003	1.993	1.818	2.103	2.026	1.749	3.428	1.868
B[c]	2	1.662	2.074	2.013	1.976	1.816	2.092	2.019	1.757	3.414	1.831
A[b]	1	1.668	2.152	2.032	1.921	1.778	2.087	2.037	1.835	3.388	1.435
B[c]	1	1.679	2.118	2.057	1.836	1.754	2.100	2.008	1.901	3.390	1.418

[a] Optimization used functional/basis (code): 1 = BPVWN/IV (ADF); 2 = B3LYP/6-311G (G'03).
[b] O_T is trans to amine and OH trans to pyridine.
[c] O_T is trans to pyridine and OH trans to amine.
[d] Average over cis pyridines.

Table S6. Selected dihedral and bond angles (in degrees) for DFT optimized structures for the S = 2 states of the isomers $[L(O_T)_{py}FeOFe(OH)_{am}L]^{3+}$ and $[L(O_T)_{am}FeOFe(OH)_{py}L]^{3+}$ (L = TPA).

iso	opt[a]	H-O-Fe_{OH}-O_B	O_{OH}-Fe_{OH}-Fe_O-O_T	Fe-O-Fe
A[b]	2	51.1	–41.1	132.6
B[c]	2	45.0	–44.7	132.2
A[b]	1	24.9	-18.1	128.9
B[c]	1	12.7	-12.9	130.2

[a] Optimization used functional/basis (code): 1 = BPVWN/IV (ADF); 2 = B3LYP/6-311G (G'03).
[b] O_T is trans to amine and OH trans to pyridine.
[c] O_T is trans to pyridine and OH trans to amine.

While *method 2* shows a *trans* effect on the Fe_O-N_{tr} distance due to the oxo group, those distances change less between the two isomers when using *method 1*. Instead, a *trans* effect is observed on the Fe_O-O_B and Fe_{OH}-O_B distances: the longest Fe-O_B distance being always the one *trans* to the N_{py}, the shortest being the one *trans* to the N_{am}. The oxo↔hydroxo *cis* ligand exchange has little effect on the Fe-O_B distances in the optimizations with *method 1*. Furthermore, Table S5 shows that, regardless the isomer, the (O)H---O_T distance is treated differently by the two methods (see below): *Method 1* favors a shorter (O)H---O_T distance (1.427 Å) compared to *method 2* (1.850 Å). Thus, in the structure obtained with *method 2*, the hydrogen atom of the OH group is closer to the

O_T and the Fe_{OH}-O(H) is shorter than in the structure obtained with *method 1*. Hence, the structural dissimilarity of Fe_O and Fe_{OH} is mitigated by *method 1*, resulting in more balanced *trans* effects for the oxo and hydroxo groups and leaving the *trans* effect of N_{am} and N_{py} on the Fe-O_B bonds as the dominant *trans* effect.

From now on, we will focus on the $[L(O_T)_{am}FeOFe(OH)_{py}L]^{3+}$ isomer for the following reason. We think this isomer is lowest in energy because it pairs the strongest O-donor (O_T) with the weakest N-donor (amine) as *trans* ligand, and vice versa. (N.B. Fe_O-O_T is shorter than Fe_{OH}-O(H), regardless of the method, on the basis of which we consider O_T to be stronger ligand than OH. Similarly, N_{py} is stronger than N_{am} since Fe-N_{py} is shorter than Fe-N_{am}.) This pairing of *trans* ligands is supported by the crystal structure of the green intermediate $[Fe_2(\mu\text{-}O)_2(5\text{-}Et_3\text{-}TPA)_2][ClO_4]_3$, which has a $Fe_2(\mu\text{-}O)_2$ diamond core of which the shortest and longest Fe-O_B distances are, respectively, *trans* to the N_{am} and N_{py}.[16] The same pairing is found for the $[Fe_2(\mu\text{-}O)_2(6\text{-}Me_3\text{-}TPA)_2][ClO_4]_2$ complex.[17, 18] We have currently not yet found a quite satisfactory explanation why *method 1* calculates isomer B as the most stable isomer while *method 2* prefers isomer A.

Table S7. Selected distances for DFT optimized structures for the S = 2 state of the $[L(O_T)_{am}FeOFe(OH)_{py}L]^{3+}$ isomer.[a]

L[b]	**opt**[b]	**Fe_O-O_T**	**Fe_O-N_{am}**	**<Fe_O-N_{py}>$_{av}$**	**Fe_O-O_B**	**Fe_{OH}-O(H)**	**Fe_{OH}-N_{am}**	**<Fe_{OH}-N_{py}>$_{av}$**	**Fe_{OH}-O_B**	**Fe-Fe**	**(O)H···O_T**
SR	1	1.670	2.125	2.029	1.891	1.778	2.054	2.039	1.843	3.395	1.501
SR	2	1.656	2.102	2.004	1.993	1.823	2.084	2.024	1.750	3.436	1.780
TPA	1	1.667	2.152	2.032	1.921	1.778	2.087	1.999	1.835	3.388	1.435
TPA	2	1.653	2.123	2.003	1.993	1.818	2.103	2.026	1.749	3.428	1.868

[a] O_T = terminal oxo; am = amine; py = pyridine; O_B = bridging oxo. Distances in Å. O_T is *trans* to amine and OH *trans* to pyridine.
[b] SR = SR_3TPA
[c] Optimization used functional/basis (code): 1 = BPVWN/IV (ADF), 2 = B3LYP/6-311G (G'03).

In Tables S7 and S8 we have listed selected geometrical parameters for the O_T-*trans*-N_{am} isomer, obtained for computational models with the complete ligand (L = SR_3TPA) and a truncated version of the ligand (L = TPA). These tables also compare the results of *method 2* with those obtained with *method 1*. The optimized structures have X-Fe-Y angles (not tabulated) that deviate from the ideal octahedral values (90°, 180°) by up to 20° (see, e.g., Figure S7). The two methods yield distances (Table S7) that differ by less than 0.03 Å, with noticeable exceptions: First, the (O)H···O_T separations differ by as

much as ~ 0.3 – 0.4 Å, and signal a significant discrepancy between the two methods in assessing hydrogen bonding or dihedral angles. [It is presently not clear whether the methodological differences in the values for the dihedral angles defined in Table S8 (see below) are caused by the difference in hydrogen bond length, or vice versa.] Second, the Fe_O-O_B and Fe_{OH}-O_B distances as obtained with *method 1* are virtually equal but differ by as much as 0.2 Å in the structures optimized with *method 2*.

The geometry optimizations show that complex **2** (L = SR_3TPA) and its truncated version (L = TPA) are chiral molecules with non-planar $O_TFe_OOFe_{OH}OH$ moieties. The dihedral angles for one of the two enantiomers are listed in Table S8; the dihedrals for the second enantiomer have reversed signs. Not surprisingly, given the large discrepancy in the hydrogen bond distance, the dihedral angles obtained with the two methods are markedly different, with *methods 1* and *2* resulting in moderate and large torsions angles, respectively. A comparison of the results for the full and truncated structures in Tables S7 and S8 reveals minor differences in the distances and somewhat more substantial discrepancies in the dihedrals.

Table S8. Selected dihedral and bond angles for DFT optimized structures for the S = 2 state of $[L(O_T)_{am}FeOFe(OH)_{py}L]^{3+}$ isomer [a]

L[b]	opt[c]	H-O-Fe_{OH}-O_B	O_{OH}-Fe_{OH}-Fe_O-O_T	Fe-O-Fe
SR	1	22.9	–19.2	130.8
SR	2	45.1	–35.0	133.1
TPA	1	24.9	–18.1	128.9
TPA	2	51.1	–41.1	132.6

[a] Angles are given in degrees. Dihedrals are reversed in sign associated enantiomer. O_T is trans to amine and OH trans to pyridine.
[b] SR = SR_3TPA.
[c] Optimization used functional/basis (code): 1 = BPVWN/IV (ADF), 2 = B3LYP/6-311G (G'03).

The Fe-O-Fe unit is bent with an angle of 131° (Table S8). To investigate the potential effect of hydrogen bonding (O)H···O_T on the Fe-O-Fe angle, we have performed a geometry optimization for a model in which the OH group was replaced by a fluoride. The substitution results in a large increase in the dihedral O_T-Fe_O-Fe_F-F to 143.9° (using *method 2* applied to the TPA complex) and a concomitant increase in the Fe-O-Fe angle to 158.6°, suggesting a possible influence of the hydrogen bond on the Fe-O-Fe angle of

2, although interference of other factors affected by the substitution cannot be excluded. The latter value is slightly larger than the bridging angle in the diiron(IV) species $[B^*FeOFeB^*]^{2-}$ (Fe-O-Fe = 153°), where the bending was shown to be an intrinsic property of the FeOFe unit.[14]

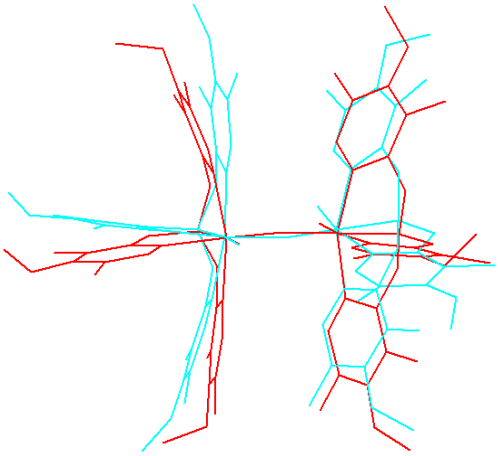

Figure S10. Overlay of the optimized geometries of **2** obtained using *method 1* (red) and *2* (blue). Hydrogen atoms have been omitted for clarity.

Table S9. Quadrupole splittings, asymmetry parameters, and spin-dipolar magnetic hyperfine coupling constants calculated for DFT optimized structures for the S = 2 state of the $[L(O)_{am}FeOFe(OH)_{py}L]^{3+}$ isomer.[a]

L[b]	opt[c,d]	prop[c,e]	Fe_O			Fe_{OH}			Fe_O			Fe_{OH}		
			δ	ΔE_Q	η	δ	ΔE_Q	η	$A_{SD,\xi}$[f]	$A_{SD,\eta}$	$A_{SD,\zeta}$	$A_{SD,\xi'}$	$A_{SD,\eta'}$	$A_{SD,\zeta'}$
SR	1	1	-	-0.80	0.75	-	2.18	0.27	-5.9	-4.0	9.8	-11.0	-3.2	14.3
SR	1	2	-	1.57	0.07	-	3.29	0.44	–6.7	–4.7	11.4	–10.1	–1.7	11.8
SR	1	3	-	–0.89	0.88	-	2.56	0.28	–4.1	–2.9	7.0	–8.0	–1.9	9.9
SR	2	2	0.05	1.31	0.50	0.03	2.69	0.22	–6.3	–5.0	11.3	–9.0	–4.5	13.6
Exp	-	-	–0.03	0.92	0	0.00	1.96	0	–6.1	–5.8	11.9	–11.0	–2.0	13.0
TPA	1	1	-	0.79	0.84	-	1.82	0.30	–6.0	–4.4	10.4	–11.4	–2.6	14.0
TPA	1	2	-	1.66	0.10	-	2.99	0.50	–6.9	–4.7	11.5	–10.1	–2.2	12.4
TPA	2	2	0.06	1.23	0.42	0.04	2.69	0.24	–6.2	–4.9	11.2	–9.0	–4.6	13.5

[a] δ and ΔE_Q in mm/s using Q(^{57}Fe) = 0.17 barn; A-values are in T.
[b] SR = SR_3TPA.
[c] Functional/basis (code): 1 = BPVWN/IV (ADF), 2 = B3LYP/6-311G (G'03), 3 = PBEVWN/6-311G (G'03).
[d] Method used for geometry optimization.
[e] Method used for calculation of properties.
[f] A-values are listed here in increasing order of their values.

Table S9 lists hyperfine parameters obtained with different methods and for both the complete (SR) and truncated ligand system (TPA). With a few exceptions, the eigenvalues of the EFG and A_{SD} tensors come out relatively constantly. The ΔE_Q values for Fe_O are consistently smaller than those for Fe_{OH}, irrespective of method or ligand truncation, in accordance with experiment. The values for ΔE_Q, predicted using $Q(^{57}Fe)$ = 0.17 barn, are systematically somewhat higher than those observed experimentally. [To accommodate this observation we proposed in ref. [19] the use of a slightly smaller value of $Q(^{57}Fe)$ for predicting the quadrupole splitting in high-valent iron complexes with *method 2*.] The calculated values for η vary over a broad range and appear to be hard to predict for this system. The calculated A_{SD} values for Fe_O are nearly axial, while those for Fe_{OH} show a significant degree of rhombicity, in accord with the Mössbauer analysis (Table S9). As expected, *methods 1* and *3* yield similar quadrupole splittings for the structure optimized with *method 1*.

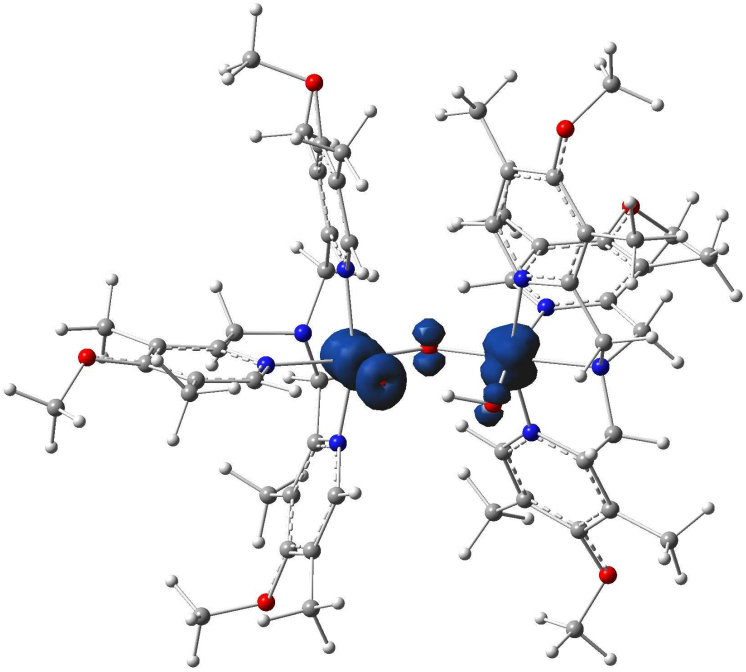

Figure S11. DFT-calculated spin density for **2**. Fe_O is on the left. The geometry has been optimized with *method 1*, and the spin density has been calculated with *method 2*.

As can be seen from the spin-density profile in Figure S11 (for SR_3TPA) the t_{2g} orbitals of Fe_{OH} are engaged in π interactions with the lone-pair p-orbitals at the hydroxide

oxygen and the bridging oxygen. As a result, the torsion angle of the hydroxide ligand has an important effect on the composition of the t_{2g} orbitals (and their energies) and related properties such as the EFG, A_{SD}, and J. Probably to a lesser degree, these properties may also be affected by the (H)O-Fe_{OH}-Fe_O-O_T torsion. Since the torsion angles are dependent on the method used for the optimization, the properties should exhibit methodological differences as well. Particularly affected are the orientations of the principal axes of the EFG and A_{SD} tensors for Fe_{OH} (not listed). In the case of small torsions, such as in the optimized structures obtained with *method 1*, the principal axes on Fe_{OH} site are expected to be roughly collinear with the metal–ligand bonds with the largest component of the two tensors being along x, whereas in the case of large torsions, as obtained with *method 2*, the ligand and tensor frames are far from collinear. [In fact, the structure optimized with *method 1* gives already rise to a considerable degree of non-collinearity between the ligand and tensor frames at Fe_{OH}, see main text.] In contrast, the dihedrals in Table S8 have little effect on the orientation of the principal axes of the tensors for Fe_O, where the z axis is invariably along the Fe_O-O_T vector. Unlike the spin density in the $d_{x'y'}$ orbital at Fe_{OH}, the spin density in the d_{yz} orbital at Fe_O exhibits only minor spin delocalization toward the oxo bridge, possibly because of sp^2 hybridization at O_B in the yz plane.

Table S10. Cartesian coordinates (Å) for the DFT energy minimized model of $[LFe^{IV}(O)(NCMe)]^{2+}$.

	x	y	z		x	y	z
N	0.014134	-0.868012	1.445520	C	-5.148141	-5.148141	-2.274662
N	-1.950651	-0.851412	-0.356916	H	-5.809854	-1.185153	-2.455059
N	1.979822	-0.816492	-0.356361	H	-5.766809	0.551000	-2.155434
N	-0.001417	1.155073	-0.344885	H	-4.556115	-0.196737	-3.177656
C	-1.239596	-1.616736	1.824698	C	-0.009663	3.494599	2.646627
H	-1.481591	-1.442088	2.871806	H	-0.861046	4.156771	2.806319
H	-1.035300	-2.681782	1.710578	H	-0.045006	2.709338	3.397828
C	-2.365888	-1.216910	0.895710	H	0.881098	4.098271	2.827215
C	-3.717007	-1.267653	1.220166	C	0.107709	4.311629	-2.400365
C	-4.662615	-0.923465	0.210415	H	0.207932	3.698666	-3.294704
C	-4.235958	-0.587651	-1.094389	H	-0.767228	4.944427	-2.542821
C	-2.858402	-0.557690	-1.309729	H	0.984855	4.958007	-2.353933
H	-2.454766	-0.315803	-2.280621	O	5.980939	-0.896729	0.658405
C	1.280834	-1.595347	1.824010	O	-5.951035	-1.022080	0.650130
H	1.095560	-2.663451	1.706398	O	-0.011940	5.185124	0.582125
H	1.518617	-1.419408	2.871855	C	7.138364	-0.184546	0.086479
C	2.400433	-1.172421	0.897352	H	6.904047	0.868563	-0.053144
C	3.751622	-1.193227	1.224670	H	7.908381	-0.295939	0.840568
C	4.691316	-0.827658	0.216881	H	7.462130	-0.645044	-0.840998
C	4.260185	-0.502538	-1.089080	C	-0.484869	6.353820	-0.181383
C	2.882855	-0.503630	-1.307552	H	-0.539528	7.141919	0.560251
H	2.476102	-0.271675	-2.279564	H	0.221895	6.628112	-0.957717
C	0.002938	0.539258	2.011668	H	-1.473378	6.163542	-0.594180
H	0.874783	0.660156	2.655124	C	-7.125958	-0.346709	0.069819
H	-0.874440	0.647762	2.649920	H	-7.895885	-0.477381	0.820896
C	-0.001200	1.601422	0.940565	H	-6.922057	0.712189	-0.073459
C	-0.011514	2.961309	1.237202	H	-7.431791	-0.820457	-0.857077
C	-0.023932	3.886175	0.159960	N	0.031637	-2.784993	-0.835644
C	0.005390	3.427643	-1.177398	C	0.042785	-3.877530	-1.223284
C	0.006752	2.047705	-1.362251	C	0.056681	-5.236026	-1.733931
H	0.028385	1.620909	-2.352299	H	0.946435	-5.402316	-2.342343
O	0.011585	-0.612511	-2.279697	H	0.056505	-5.960034	-0.918566
C	4.281056	-1.594857	2.577370	H	-0.821921	-5.415709	-2.354623
H	4.904691	-0.804392	2.995210	Fe	0.014080	-0.786915	-0.635539
H	3.494220	-1.826127	3.290547				
H	4.923816	-2.472158	2.490177				
C	5.169919	-0.233196	-2.266852				
H	5.766158	0.670403	-2.147872				
H	5.852835	-1.065064	-2.442403				
H	4.577898	-0.109563	-3.172336				
C	-4.239713	-1.681253	2.571903				
H	-3.448981	-1.895707	3.286023				
H	-4.880882	-0.904646	2.989223				
H	-4.863222	-2.572207	2.483475				

Table S11. Cartesian coordinates (Å) for the DFT energy minimized model of **2** using *method 2*.

	x	y	z
Fe	1.686713	-0.093563	-0.123498
O	-0.266471	-0.073482	0.274568
N	2.197812	0.253149	1.885571
N	1.700432	1.894987	-0.178285
N	1.915630	-1.980255	0.515101
N	3.675654	-0.016435	-0.348601
C	1.619315	1.597237	2.216500
H	2.062680	1.989144	3.130029
H	0.556176	1.447326	2.398199
C	1.802684	2.523553	1.035327
C	2.002707	3.897305	1.121477
C	2.085175	4.638024	-0.093138
C	1.914920	4.000707	-1.339704
C	1.743711	2.615628	-1.314977
H	1.605735	2.061416	-2.227713
C	1.553259	-0.888667	2.626391
H	0.479996	-0.708978	2.611588
H	1.891381	-0.916072	3.661216
C	1.879456	-2.158418	1.872903
C	2.162680	-3.393166	2.448420
C	2.541031	-4.461373	1.584079
C	2.578507	-4.279854	0.183737
C	2.250523	-3.008585	-0.290001
H	2.241290	-2.793880	-1.347261
C	3.699999	0.238144	2.068298
H	3.966215	-0.624104	2.682616
H	3.998998	1.121136	2.634867
C	4.437595	0.172078	0.758693
C	5.826461	0.271063	0.694418
C	6.444098	0.172962	-0.579178
C	5.657530	-0.056033	-1.734219
C	4.278921	-0.129639	-1.555572
H	3.615250	-0.307012	-2.386780
Fe	-1.687143	0.164073	-0.719672
O	-0.813296	0.740485	-2.211766
N	-3.395858	0.436003	-1.881791
N	-1.857079	-1.688312	-1.462827
N	-2.161588	2.074569	-0.238941
N	-3.066253	-0.429553	0.666347
C	-3.233960	-0.505874	-3.048960
H	-4.186354	-0.633663	-3.562686
H	-2.524109	-0.044661	-3.731882
C	-2.674237	-1.808740	-2.547329
C	-2.930382	-3.045754	-3.149863
C	-2.384658	-4.187735	-2.528588
C	-1.556785	-4.070103	-1.392658
C	-1.310498	-2.792824	-0.903785
H	-0.676964	-2.624558	-0.050194
C	-3.321625	1.874294	-2.333390
H	-2.525481	1.929925	-3.072224
H	-4.265707	2.176441	-2.786049

C	-2.953146	2.714442	-1.143430
C	-3.363326	4.040749	-0.963646
C	-2.986804	4.672843	0.238729
C	-2.190243	4.007253	1.192019
C	-1.795722	2.706735	0.897703
H	-1.189518	2.136612	1.580016
C	-4.656015	0.158646	-1.090667
H	-5.243794	1.075971	-1.044165
H	-5.258343	-0.567650	-1.636925
C	-4.375617	-0.342859	0.308020
C	-5.398033	-0.699443	1.185014
C	-5.043064	-1.165696	2.478715
C	-3.683390	-1.243062	2.862659
C	-2.746662	-0.867666	1.902139
H	-1.689958	-0.896222	2.116123
O	1.488500	-0.446173	-1.729615
H	-0.027946	0.182136	-2.417351
C	-1.787527	4.693542	2.468449
H	-1.285127	5.637875	2.258514
H	-2.657289	4.933780	3.082164
H	-1.123925	4.067198	3.063583
C	-4.133110	4.785685	-2.027899
H	-5.210232	4.607243	-1.967755
H	-3.970757	5.856237	-1.923535
H	-3.809452	4.506134	-3.029633
O	-3.290177	5.995464	0.485376
C	-4.675578	6.409732	0.810939
H	-4.614261	7.482137	0.950220
H	-5.358294	6.175617	-0.002830
H	-4.997704	5.926998	1.732235
C	-3.191914	-1.625654	4.240450
H	-3.607220	-0.974167	5.010077
H	-3.431615	-2.653154	4.510376
H	-2.107599	-1.527484	4.288354
C	-6.859215	-0.607745	0.829184
H	-7.370157	0.101112	1.483033
H	-7.027642	-0.300469	-0.199954
H	-7.352890	-1.567480	0.983379
O	-6.132289	-1.449942	3.251015
C	-6.174217	-2.351080	4.417386
H	-5.708513	-1.893633	5.284468
H	-7.233410	-2.487055	4.600355
H	-5.714470	-3.307191	4.175792
C	-3.699381	-3.147451	-4.445917
H	-3.382078	-4.028612	-4.999779
H	-4.779105	-3.222260	-4.291490
H	-3.517865	-2.287211	-5.088426
C	-0.973941	-5.296348	-0.745777
H	-1.758972	-5.953151	-0.367254
H	-0.404123	-5.880720	-1.468490
H	-0.324342	-5.031431	0.086740
O	-2.534148	-5.453725	-3.048389
C	-3.855412	-6.120522	-3.113787
H	-4.543970	-5.581891	-3.759309
H	-3.644194	-7.098026	-3.529873
H	-4.265721	-6.217689	-2.109850

C	2.104347	-3.663050	3.930156
H	1.413736	-4.480740	4.139471
H	3.075657	-3.988150	4.305091
H	1.784902	-2.797952	4.505347
C	2.885809	-5.368487	-0.818530
H	3.923892	-5.697416	-0.777676
H	2.254301	-6.244287	-0.668818
H	2.705118	-5.007431	-1.829876
C	2.149964	4.650679	2.419570
H	3.122508	5.142396	2.467679
H	1.409261	5.447153	2.487703
H	2.044887	4.016073	3.295355
C	1.841273	4.711124	-2.671756
H	1.082279	5.494200	-2.663638
H	2.786300	5.166881	-2.965410
H	1.568550	4.005218	-3.454684
C	6.652177	0.468181	1.941462
H	7.701147	0.568254	1.687029
H	6.351036	1.364888	2.489374
H	6.559416	-0.381027	2.623945
C	6.222214	-0.307638	-3.113279
H	5.429157	-0.616466	-3.792513
H	6.692206	0.574044	-3.548137
H	6.964746	-1.106319	-3.097071
O	2.786766	-5.625029	2.255679
O	2.268526	5.976442	0.116043
O	7.808466	0.244832	-0.550135
C	3.726846	-6.685555	1.835880
H	4.663904	-6.248104	1.498197
H	3.889774	-7.260887	2.739411
H	3.286743	-7.316956	1.071240
C	8.658935	0.819583	-1.611813
H	9.590757	1.046822	-1.107432
H	8.835911	0.097290	-2.401884
H	8.213941	1.732636	-2.002572
C	2.930035	6.912044	-0.814345
H	3.152703	7.776298	-0.199859
H	3.852707	6.478703	-1.194975
H	2.264480	7.196320	-1.622730

Table S12. Cartesian coordinates (Å) for the DFT energy minimized model of **2** (isomer A) using *method 1*.

	x	y	z
Fe	1.703934	-0.193344	1.053879
Fe	-1.586243	-0.278564	0.223160
O	0.274506	-0.219589	-0.109100
O	-1.586243	-0.279007	1.893082
O	0.811600	-0.774429	2.477432
H	-0.181458	-0.566818	2.335480
N	3.345184	-0.143036	2.287628
C	2.957900	0.767563	3.413956
C	3.529100	-1.546127	2.771408
C	2.338287	1.997070	2.811508
C	3.345000	-2.474060	1.605057
C	2.445679	3.271622	3.382568
C	4.039459	-3.676453	1.472809
C	1.945084	4.354965	2.630417
C	3.783478	-4.462830	0.318771
C	1.375900	4.144943	1.355942
C	2.872635	-3.999039	-0.663589
C	1.244019	2.825012	0.923950
C	2.215057	-2.794495	-0.403336
N	2.424957	-2.049164	0.695923
N	1.690155	1.770905	1.637344
C	4.558075	0.365952	1.552658
C	4.306091	0.633057	0.084656
C	5.342804	1.083405	-0.750320
C	5.027954	1.286652	-2.112457
C	3.700180	1.116928	-2.575546
C	2.757706	0.691330	-1.649292
N	3.044617	0.440170	-0.355896
C	3.063583	3.490936	4.741287
C	5.031021	-4.129135	2.518768
O	1.935593	5.610367	3.170197
O	4.548187	-5.575760	0.190109
C	0.908203	5.306305	0.523590
C	2.673706	-4.679016	-1.996078
C	6.708572	1.407272	-0.197403
O	5.933075	1.757065	-3.013200
C	3.345337	1.400833	-4.009995
C	3.072311	6.472458	2.880890
C	7.079102	0.921692	-3.350113
C	3.960724	-6.865295	-0.138947
H	3.830032	1.006989	4.037888
H	2.218750	0.228745	4.020691
H	4.507751	-1.665237	3.254471
H	2.744125	-1.735870	3.514725
H	0.772583	2.590836	-0.028702
H	1.506927	-2.383438	-1.121094
H	4.898849	1.291977	2.038971
H	5.375061	-0.362076	1.661514
H	1.717926	0.522995	-1.927109
H	2.756882	4.466431	5.132828
H	4.163712	3.481888	4.695740

H	2.751755	2.722794	5.460205
H	5.451736	-5.100693	2.249557
H	4.558655	-4.219437	3.507187
H	5.869308	-3.422104	2.613007
H	0.420837	4.968506	-0.396942
H	1.748810	5.951523	0.234970
H	0.210617	5.937012	1.091660
H	2.222427	-3.984650	-2.716049
H	2.020065	-5.559464	-1.924118
H	3.636444	-5.008636	-2.409103
H	7.232666	2.105591	-0.858887
H	7.336319	0.510086	-0.082794
H	6.637878	1.881729	0.790512
H	2.286896	1.190094	-4.207504
H	3.953568	0.797714	-4.696854
H	3.547363	2.451645	-4.260498
H	2.828690	7.436951	3.335022
H	3.209686	6.596649	1.798248
H	3.989044	6.068436	3.331955
H	7.730072	1.554977	-3.959045
H	6.743027	0.056168	-3.936691
H	7.618683	0.582718	-2.458405
H	4.787704	-7.576035	-0.052750
H	3.562683	-6.893387	-1.158142
H	3.177841	-7.114517	0.589600
N	-1.998611	-0.269714	-1.861679
C	-1.334152	0.968170	-2.356003
C	-1.375702	-1.530655	-2.359451
C	-1.663757	2.088425	-1.395676
C	-1.758072	-2.637680	-1.405334
C	-1.851837	3.420227	-1.785049
C	-2.116409	-3.929077	-1.811417
C	-2.200195	4.343262	-0.770645
C	-2.520737	-4.834534	-0.802078
C	-2.315109	3.934494	0.574661
C	-2.499619	-4.456909	0.558090
C	-2.071091	2.590561	0.856674
C	-2.102615	-3.150650	0.852753
N	-1.755814	-2.259735	-0.097778
N	-1.755463	1.695526	-0.097778
C	-3.479385	-0.242065	-2.143768
C	-4.320236	-0.184372	-0.892548
C	-5.713608	-0.074402	-0.958420
C	-6.432526	-0.046234	0.263641
C	-5.734406	-0.100494	1.497269
C	-4.347305	-0.209335	1.429825
N	-3.651794	-0.253647	0.274536
C	-1.654617	3.873367	-3.212204
C	-2.091736	-4.357086	-3.260239
O	-2.310852	5.674362	-1.059509
O	-2.847794	-6.115707	-1.149658
C	-2.646835	4.915863	1.664322
C	-2.882828	-5.422729	1.646591
C	-6.427017	0.021408	-2.283508
O	-7.771698	0.152542	0.158310
C	-6.391846	0.052063	2.846466

C	-3.589249	6.128800	-1.594696
C	-8.710754	-0.725693	0.840103
C	-4.265884	-6.397598	-1.336472
H	-1.636826	1.202118	-3.385834
H	-0.253494	0.776016	-2.342972
H	-1.679916	-1.748184	-3.392258
H	-0.287811	-1.378036	-2.339249
H	-2.121506	2.200851	1.872604
H	-2.067917	-2.786469	1.878891
H	-3.705460	0.621704	-2.786500
H	-3.745819	-1.137009	-2.726349
H	-3.740906	-0.233810	2.334854
H	-1.496841	4.957031	-3.240631
H	-2.531250	3.649551	-3.839249
H	-0.783417	3.394485	-3.677429
H	-2.240646	-5.439133	-3.328522
H	-1.135345	-4.117249	-3.743637
H	-2.890045	-3.873352	-3.843903
H	-2.530777	4.463562	2.655716
H	-3.681244	5.276352	1.571976
H	-1.998886	5.799133	1.594925
H	-2.638443	-5.024109	2.637802
H	-2.369919	-6.383331	1.508560
H	-3.961884	-5.634140	1.627900
H	-7.506622	0.092575	-2.129852
H	-6.225647	-0.855179	-2.917419
H	-6.111511	0.914612	-2.844543
H	-5.649673	0.336960	3.602142
H	-6.862350	-0.881088	3.187820
H	-7.166885	0.828995	2.819473
H	-3.466583	7.201431	-1.768555
H	-4.392776	5.957214	-0.865738
H	-3.823883	5.621872	-2.540833
H	-9.697830	-0.320953	0.599472
H	-8.570557	-0.725769	1.925200
H	-8.617355	-1.744812	0.441391
H	-4.326614	-7.468918	-1.547440
H	-4.662521	-5.826706	-2.188568
H	-4.839966	-6.164459	-0.429672

References

1. Shan, X.; Que, L., Jr., High-valent nonheme iron-oxo species in biomimetic oxidations. *J. Inorg. Biochem.* **2006,** 100, (4), 421-33.
2. M. J. Frisch *et al. Gaussian 03, Revision E.01*, 2004.
3. Vrajmasu, V.; Münck, E.; Bominaar, E. L., Density functional study of the electric hyperfine interactions and the redox-structural correlations in the cofactor of nitrogenase. Analysis of general trends in Fe-57 isomer shifts. *Inorg. Chem.* **2003,** 42, (19), 5974-5988.
4. Rohde, J. U.; Torelli, S.; Shan, X.; Lim, M. H.; Klinker, E. J.; Kaizer, J.; Chen, K.; Nam, W.; Que, L., Structural Insights into Nonheme Alkylperoxoiron(III) and

Oxoiron(IV) Intermediates by X-Ray Absorption Spectroscopy. *J. Am. Chem. Soc.* **2004,** 126, 16750-16761.
5. f is the Debye-Waller factor, $f = \exp\{-E_\gamma^2 \langle x^2 \rangle / (\hbar c)^2)\}$ where $E_\gamma = 14.37$ KeV and $\langle x^2 \rangle$ the mean square vibrational amplitude along direction x.
6. Mclean, P. A.; Papaefthymiou, V.; Ormejohnson, W. H.; Münck, E., Isotopic Hybrids of Nitrogenase - Mossbauer Study of Mofe Protein with Selective Fe-57 Enrichment of the P-Cluster. *J. Biol. Chem.* **1987,** 262, (27), 12900-12903.
7. ADF2008.01 (SCM, Theoretical Chemistry, Vrije Universiteit, Amsterdam, The Netherlands, http://www.scm.com).
8. Vosko, S. H.; Wilk, L.; Nusair, M., *Can. J. Phys.* **1980,** 58, 1200.
9. Becke, A. D., *J. Chem. Phys.* **1986,** 84, 4524-4529.
10. Perdew, J. P., *Phys. Rev. B.* **1986,** 33, 8822-8824.
11. Becke, A. D., *J. Chem. Phys.* **1993,** 98, 5648.
12. Lee, C.; Yang, W.; Parr, R. G., *Phys. Rev. B.* **1988,** 37, 785.
13. Catlett, C., *"TeraGrid: Analysis of Organization, System Architecture, and Middleware Enabling New Types of Applications", HPC and Grids in Action*. Lucio Grandinetti, IOS Press ed.; Amsterdam, 2007.
14. Chanda, A.; de Oliveira, F. T.; Collins, T. J.; Münck, E.; Bominaar, E. L., Density Functional Theory Study of the Structural, Electronic, and Magnetic Properties of a mu-oxo Bridged Dinuclear Fe-IV Complex Based on a Tetra-Amido Macrocyclic Ligand. *Inorg. Chem.* **2008,** 47, (20), 9372-9379.
15. Decker, A.; Solomon, E. I., Comparison of Fe-IV = O heme and non-heme species: Electronic structures, bonding, and reactivities. *Angew. Chem. Int. Ed.* **2005,** 44, (15), 2252-2255.
16. Hsu, H. F.; Dong, Y. H.; Shu, L. J.; Young, V. G.; Que, L., Crystal Structure of a Synthetic High-Valent Complex with an $Fe_2(\mu\text{-}O)_2$ Diamond Core. Implications for the Core Structures of Methane Monooxygenase Intermediate **Q** and Ribonucleotide Reductase Intermediate **X**. *J. Am. Chem. Soc.* **1999,** 121, (22), 5230-5237.
17. Zheng, H.; Zang, Y.; Dong, Y. H.; Young, V. G.; Que, L., Complexes with $Fe^{III2}(\mu\text{-}O)(\mu\text{-}OH)$, $Fe^{III2}(\mu\text{-}O)_2$, and $[Fe^{III3}(\mu_2\text{-}O)_3]$ cores: Structures, Spectroscopy, and Core Interconversions. *J. Am. Chem. Soc.* **1999,** 121, (10), 2226-2235.
18. Zang, Y.; Dong, Y. H.; Que, L.; Kauffmann, K.; Münck, E., The First Bis(Mu-Oxo)Diiron(Iii) Complex - Structure and Magnetic-Properties of [Fe-2(Mu-0)(2)(6Tla)(2)](Clo4)(2). *J. Am. Chem. Soc.* **1995,** 117, (3), 1169-1170.
19. Chanda, A.; Shan, X.; Chakrabarti, M.; Ellis, W. C.; Popescu, D. L.; Tiago de Oliveira, F.; Wang, D.; Que, L., Jr.; Collins, T. J.; Münck, E.; Bominaar, E. L., (TAML)FeIV O complex in aqueous solution: synthesis and spectroscopic and computational characterization. *Inorg. Chem.* **2008,** 47, (9), 3669-78.